Acta Materialia 232 (2022) 117941

Contents lists available at ScienceDirect

Acta Materialia

journal homepage: www.elsevier.com/locate/actamat

Enhanced mobility of cations and anions in the redox state: The polaronium mechanism

Yanhao Dong[a], Liang Qi[b], Ana Alvarez[c], Ju Li[a,d], I-Wei Chen[c,*]

[a] Department of Nuclear Science and Engineering, Massachusetts Institute of Technology, Cambridge, MA 02139, USA
[b] Department of Materials Science and Engineering, University of Michigan, Ann Arbor, MI 48109, USA
[c] Department of Materials Science and Engineering, University of Pennsylvania, 3231 Walnut St., Philadelphia, PA 19104, USA
[d] Department of Materials Science and Engineering, Massachusetts Institute of Technology, Cambridge, MA 02139, USA

ARTICLE INFO

Article history:
Received 4 December 2021
Revised 4 April 2022
Accepted 12 April 2022
Available online 14 April 2022

Keywords:
Polarons
Diffusion
Defects
Oxides
Electronic structure
Electron-phonon coupling
First-principles calculations
Zirconia
$BaTiO_3$
Li-rich layered cathode

ABSTRACT

Hugely enhanced slow-ion diffusivity has been widely observed under extreme redox conditions and for unclear reasons. Aided by first-principles calculations on model systems of ZrO_2, CeO_2, $BaTiO_3$ and $Li_{4/3}Mn_{2/3}O_2$, here we successfully explained the intriguing phenomenon by a polaronium mechanism. We found a polaronium, defined as a transitory complex of a polaronic electron or hole and a migrating counterion, becomes highly mobile when the counterion comes from a d^0 or f^0 cation (e.g., Zr^{4+}, Ti^{4+} and Ce^4) or a p^6 anion (e.g., O^{2-}) in the host compound. Upon a redox reaction, the complex attains a d^1/f^1 or p^5 configuration, which spontaneously forms because it is favored by an electron-phonon interaction (manifest as the Jahn-Teller effect in high symmetry systems) that enables local relaxation and lowers the system energy. Our calculations found such interaction reaching its peak at the saddle point where the local environment is softest, so soft that it allows a reorientation of the anisotropic *d*/*f*/*p* orbital to minimize the electron repulsion locally. Since the complex may dissolve after a successful ion-migration event, the redox electron/hole can be recycled to form another free-radical-like polaronium elsewhere, thereby enhancing ion migration repeatedly. The proposed polaronium mechanism, which also operates in ceramics doped with mixed-valence cations, is most relevant under dynamic and extreme thermal/field/irradiation conditions where extra electrons/holes are abundantly generated by non-equilibrium redox reactions. For such operations, some with emerging applications, our diffusion-enhancing mechanism may provide new theoretical insight to help understand their material/microstructure stability and performance.

1. Introduction

Recent years have seen increasing evidence that extreme redox conditions can render some ions hugely mobile in electrochemical materials and devices [1–7]. Empirically, the enhanced mobilities may be assigned to reduced cations [1–4] and oxidized anions [5–7], suggesting the same phenomenon may also occur when using aliovalent dopants to tune the redox states. The standard argument of redox-altered concentrations of ion vacancies fails to explain these findings, since oxidation generally suppresses anion vacancies thus cannot make oxidized anions diffuse faster, and reduction generally suppresses cation vacancies thus cannot make reduced cations diffuse faster. Although the opposite conclusion applies if interstitials are to dominate ion diffusion, the interstitial mechanism is relatively uncommon and highly unlikely in all the cases referenced above. Here we will explain why reduced cations and oxidized anions can migrate faster by a fundamentally new transport mechanism. The ion types seeing the most effect will be identified.

In the redox state of a polar material, lattice defects and impurities often trap some of the extra electrons and holes, which move by thermally activated hopping with an activation energy as high as 0.5–1 eV. This holds even when the mobility of the remaining untrapped electrons and holes still decreases with increasing temperature, although they too are much slower than typical band electrons and holes because of long-range Coulomb interactions. For this reason, the latter electronic carriers are called large polarons, in contrast to small polarons—such as the trapped ones mentioned above—that experience mostly localized interactions and migrate by thermal activation [8]. Against this background comes our surprising discovery in the same polaronic material: despite its larger size a redox ion dressed with a small polaron hops in and out of a neighboring vacant site much easier than an undressed ion! Below we will demonstrate that the enhanced mobility of a dressed redox ion originates in a quantum

* Corresponding author.
E-mail address: iweichen@seas.upenn.edu (I.-W. Chen).

https://doi.org/10.1016/j.actamat.2022.117941
1359-6454/

mechanical effect on the ion/small-polaron complex. To emphasize this point, we will call such complex a "polaronium" and the new migration mechanism a polaronium mechanism.

We will use these terms only when the complex comprises a migrating ion. (Therefore, an electron associated with a non-migrating lattice ion is just a small polaron and not a polaronium.) With "-onium" being a bound state of a particle and its antiparticle, the coined word "polaronium" is in analogy to positronium, which is a transitory positron-electron complex temporarily behaving like an atom. This analogy is apt because (a) the complexes of interest here, between a polaronic electron and a migrating cation or between a polaronic hole and a migrating anion, are too made of two charged particles of opposite signs, and (b) the complexes are also transient ones. These important features will become clear below.

2. Methods

We conducted first-principles calculations based on density functional theory (DFT) using the projector augmented-wave (PAW) method within the Perdew-Burke-Ernzerhof (PBE) generalized gradient approximation (GGA), implemented in the Vienna *ab initio* simulation package (VASP) [9–11]. The PAW potentials include the following electrons: $5s^2 4d^2$ for Zr, $5s^2 5p^6 4f^1 5d^1 6s^2$ for Ce, $5s^2 5p^6 6s^2$ for Ba, $3s^2 3p^6 3d^2 4s^2$ for Ti, $2s^1$ electron for Li, $3d^5 4s^2$ electrons for Mn, and $2s^2 2p^4$ for O. A plane-wave cutoff energy of 400 eV was used and the Brillouin zone was sampled using the Monhorst-Pack scheme with a $3 \times 3 \times 3$ k-point mesh. The DFT+U approach by Dudarev et al. [12] was used to describe the energy of localized 4d electrons of Zr, 4f electrons of Ce, and 3d electrons of Ti and Mn. Specifically, we chose the on-site Coulomb interaction parameter U, the on-site exchange interaction parameter J, and the effective Hubbard parameter U_{eff}=U–J as follows: U = 5 eV, J = 1 eV and U_{eff}=4 eV for Zr 4d states [13], U = 5 eV, J = 0 eV and U_{eff}=5 eV for Ce 4f states [14], U = 5 eV, J = 0.64 eV and U_{eff}=4.36 eV for Ti 3d states [15], and U = 3.9 eV, J = 0 eV and U_{eff}=3.9 eV for Mn 3d states [16]. (Note that Dudarev et al. did not treat U and J independently, only their difference U_{eff}=U–J is meaningful.)

All calculations were performed under periodic boundary conditions. For the ground state, we used a $2 \times 2 \times 2$ supercell containing 32 Zr or Ce and 64 O for cubic ZrO_2 and CeO_2, respectively, a $3 \times 3 \times 3$ supercell containing 27 Ba, 27 Ti and 81 O for cubic $BaTiO_3$, and a $2 \times 2 \times 1$ supercell containing 32 Li, 16 Mn and 48 O for Li_2MnO_3. Cation migration was studied via a vacancy mechanism because the Schottky reaction, having a much lower defect formation energy than cation Frenkel reaction, provides much more cation vacancies than interstitials in ZrO_2, Y-doped ZrO_2, CeO_2 and $BaTiO_3$ [17–19]. The cation vacancies and other assisting lattice defects included all have their formal charges (-4 for V_{Zr}, V_{Ce}, and V_{Ti}, -2 for V_{Ba}, and $+2$ for V_O) so that they do not affect the redox state. Oxygen ion migration was also studied via a vacancy mechanism ($+2$ for V_O) because interstitials are again energetically too costly in close-packed Li_2MnO_3. To simulate the migration of a reduced cation, we added an extra electron into the supercell, preselected a target cation next to the cation vacancy and promoted electron localization around it at the ground state by first displacing the neighboring oxygen ions outward by 0.1–1.0 Å, then letting the system relax to reach convergence (residue atomic forces less than 0.05 eV/Å). To simulate an oxidized oxygen ion, we removed an electron (i.e., adding a hole) from the supercell and did not use any extra treatments for localization.

To track cation migration, the climbing-image nudged-elastic-band (NEB) method [20] implemented in VASP was used with a fixed supercell size and shape. In cubic ZrO_2 and $BaTiO_3$, it determined the migration path and the barrier with the path defined by 7 intermediate states in addition to the initial and final configurations; in CeO_2, 3 intermediate states were used. Oxygen migration calculations were conducted using the solid-state dimer method [21], after pre-screening using the NEB method. Convergence for NEB and dimer calculations was considered achieved when the residual atomic forces were less than 0.1 eV/Å. Throughout the migration, the supercell carries the same charge and VASP adds an opposite charge to the background, so the same leading error term of electrostatic interaction remains unchanged and does not affect the energy difference between the saddle point and the ground state. (No monopole dipole or quadrupole corrections were applied.) The density of states (DOS) as well as projected DOS (pDOS), band-decomposed charge densities within certain energy ranges, and Bader charges [22] were calculated for atoms in the ground-state (L) and the saddle-point (SD) configurations. Atomic structures were visualized using VESTA [23].

3. Reduced Zr cation in [110] migration in cubic ZrO_2

Since there is unmistaken evidence of enhanced cation mobility of up to 3 orders of magnitude in reduced Y_{Zr}-doped ZrO_2 (measured at 1200–1500 °C) [1,2,24], we first study the electron distribution and the total energy of this system during Zr^{3+}([Kr]4d^1)/Zr^{4+}([Kr]4d^0) migration. This technologically important ceramic is highly stable because of copious V_O that comes with Y doping, thus the material is commonly called yttria-stabilized zirconia (YSZ). As schematically shown in a representative supercell in **Fig. 1a,** which contains a V_O, the L and the SD environments around the migrating Zr (for [110] migration) may be described by ZrO_7 and ZrO_5, respectively. This holds for both Zr^{3+} and Zr^{4+}. (Zr^{SD} in **Fig. 1** may attract a further-away oxygen ion O6 to adopt a ZrO_6 environment, which is justified by bond lengths given in the figure caption.)

In our calculation, we made Zr^{3+} possible by adding an extra electron in the supercell. This electron may be visualized in Fig. 1b–e using the band-decomposed charge densities for those bands just beneath the Fermi level E_F. In all cases, they occupy gap states, which have a relatively narrow band width indicative of electron localization as expected for a small polaron. The extra electron occupies the Zr 4$d_{x^2-y^2}$ orbital in L (Fig. 1b and c) and 4d_{xy} in SD (Fig. 1d–e), where the characteristic x-y-z axes (directed by the oxygen ligand field around the cation) are outlined by dashed lines. (At SD, z||[001], along O1-V_O-O6 in **Fig. 1a**.) Clearly, despite the larger size of the electron-dressed cation, the extra electron stays with the migrating cation. So, the ion-small-polaron complex is robust, the polaronium remains intact, and the polaronium mechanism does operate as an ion migration mechanism. Fig. 1b–e also reveals how the size effect on migration is obviated: since the dressed electron is mostly a d-electron and does not have a spherical shape, it can orient itself to take advantage of the anisotropic environment of Zr^{SD}. Specifically, as the Zr ion migrates along the [110] direction within the x-y plane, which is perpendicular to the z axis (along [001]) in Fig. 1d and e, the electron cloud is extended in the same x-y plane and suppressed along the z axis. That is, during the SD passage, the extra electron cloud seeks to avoid impinging those of neighboring oxygens (O1 and O6 in Fig. 1a) that constrict the SD landscape the most, hence defining its "hard" direction z; meanwhile, it spreads along the two "soft" directions (x and y) thus obviating the size effect.

In the presence of a V_O, the migration barrier in Table 1 for Zr^{3+} (3.17 eV) is 1.14 eV lower than that for Zr^{4+} (4.31 eV). This agrees with the experimental finding that the reduced cation has a higher mobility despite its larger ionic radius. One reason for barrier lowering is the lower energy, by 1.7 eV, of the occupied d orbital in the SD state compared to the L state. The estimate is obtained from Fig. 1f, which plots electron's pDOS for Zr^L and Zr^{SD} versus

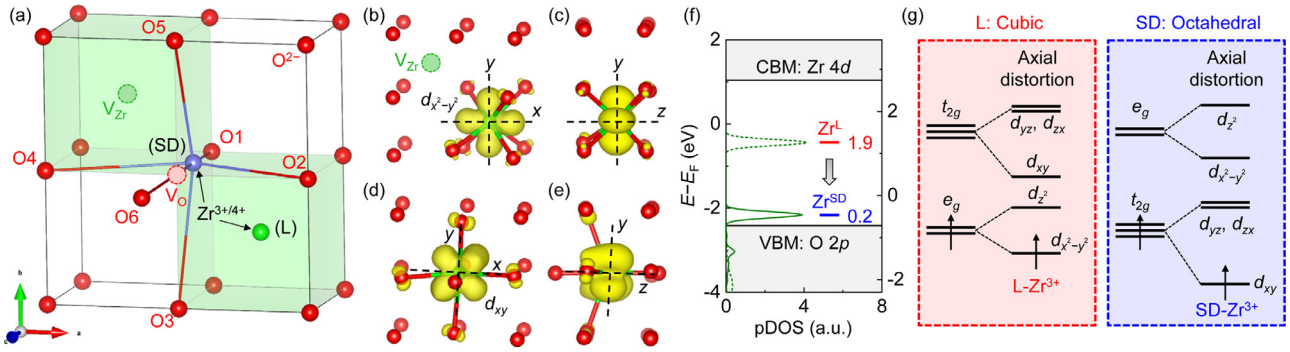

Fig. 1. **(a)** Schematic atomic structure for Zr ions at the ground state (L) and saddle point state (SD) on the way to V_{Zr} in [110] migration in cubic ZrO_2. Zr^L and V_{Zr} in green, Zr^{SD} in purple, and O and V_O in red. O1-O5 form a square pyramid. O6 is further away though pulled in by Zr^{SD}. **(b–e)** Band-decomposed charge densities of Zr^{3+} at L (b) and SD (d). (c) shows side view of (b), both with z|||[001]. (e) shows side view of (d), both with z|||[001]. One band is included, and the iso-surface is plotted with a charge density of 0.006 electron/Bohr^3. **(f)** Corresponding occupied pDOS below E_F of migrating Zr^{3+} at L (dotted curve) and SD (solid curve). Energy in eV relative to E_F is given by the left y-axis for L and the right y-axis for SD. Short bars indicate peak L and SD energy levels in eV relative to VBM. **(g)** Schematic ligand field splitting of Zr 4d orbitals at L (cubic symmetry with axial distortion) and SD (octahedral symmetry with more axial distortion). The octahedral assignment to the latter is justified because, the shortest bond of Zr^{SD}-O1 (2.11 Å) is followed by the Zr^{SD}-O6 bond (2.21 Å), followed by four other bonds between Zr^{SD} and O2–O4 (2.56 Å, 2.59 Å, 2.61 Å and 2.65 Å). Therefore, all six oxygens above must be included in the SD ligand field. Band-decomposed charge densities of Zr^{3+} in (d–e) are consistent with the shape of d_{xy}, which confirms the octahedral field splitting. (For interpretation of the references to colour in this figure legend, the reader is referred to the web version of this article.)

Table 1
Calculated migration barriers and Bader charges for V_O-assisted Zr [110] migration in cubic ZrO_2, V_O-assisted Ce [110] migration in CeO_2, V_{Ba}-assisted Ti [110] and V_O-assisted Ti [100] migration in cubic $BaTiO_3$, and O migration in Li_2MnO_3.

		Migrating ion	Migration barrier (eV)	Bader charge (e) L	SD
ZrO_2		Zr^{3+}	3.17	1.43	1.49
		Zr^{4+}	4.31	0.59	0.68
CeO_2		Ce^{3+}	3.28	1.91	1.92
		Ce^{4+}	3.96	1.65	1.67
$BaTiO_3$	[110]	Ti^{3+}	2.60	1.96	2.11
		Ti^{4+}	3.53	1.75	1.83
	[100]	Ti^{3+}	6.53	1.81	2.18
		Ti^{4+}	7.75	1.80	1.87
Li_2MnO_3		O^-	2.33	7.40	7.05
		O^{2-}	3.00	7.41	7.35

energy. Here, to compare Zr^L and Zr^{SD}, we aligned their respective valence band maximum (VBM), which in both cases corresponds to the top of the O-2p orbitals. (We chose this reference because the ZrO_2 structure comprises of cation polyhedra surrounded by O anions that are interconnected into a continuous three-dimensional network; as such, the O-2p manifolds should be rather representative of network's electronic state and relatively insensitive to the perturbations caused by an isolated defect or distortion, e.g., V_O and Zr migration. Alternatively, we could align the energy level at the average energy of O-2p orbitals, which will shift the reference energy level but not the energy difference, hence giving the same estimate.) Since the energy lowering in Fig. 1f comes from the gap states, clearly it is due to the extra electron.

The above point may be better understood using the schematic of ligand-field splitting in Fig. 1g, shown for the gap state, Zr $4d_{x^2-y^2}$ in L and $4d_{xy}$ in SD. In L, Zr^L experiences a modestly distorted cubic ligand field and the dressed electron occupies $4d_{x^2-y^2}$ orbital. In SD, Zr^{SD} experiences a more distorted octahedral ligand field because of compression along z (see bond lengths in figure captions), and the dressed electron occupies $4d_{xy}$ orbital with a lower energy level than $4d_{x^2-y^2}$ in L. This helps lowering the total energy of the saddle-point state. In contrast, without any extra 4d electron, the highest occupied molecular orbital (HOMO) of Zr^{4+} is always set at the VBM, so a migrating Zr^{4+} has no gap state thus no energetic benefit to drawn on. This explains why the polaronium mechanism can lower the migration barrier of Zr^{3+} relative to Zr^{4+}. It also explains why the size effect is not an issue: the ligand-field theory always directs cation's d-orbital away from the surrounding oxygens, so the size effect is mostly obviated.

4. Reduced Ti cation in [110] migration in cubic $BaTiO_3$

The corresponding problem of Ti^{3+} ([Ar]3d^1)/Ti^{4+}([Ar]3d^0) migration in the [110] direction in cubic $BaTiO_3$ is next studied and summarized in Fig. 2. In this schematic of the ABO_3 perovskite, the primary cell is plotted with A=Ba at the body center, B=Ti at the corners and O at the edge centers. Also included is an A-site vacancy, V_{Ba}, which facilitates [110] migration [25] and is readily available in almost all such perovskites. The figure shows that Ti^L has a slightly distorted TiO_6 configuration, and Ti^{SD} a TiO_3 configuration. The latter is surprising since the SD does not reside on the half plane perpendicular to the migration path. Instead, the midpoint of the curved migration path with Ti placed inside a puckered square pyramid of TiO_4V_{Ba} (not shown) proves to be a local minimum, and there are two local maxima (SD) on two sides of the midpoint, each with a Ti^{SD} near the center of $V_{Ba}O_3$ so that $Ti^{SD}O_3$ almost flattens into a triangular plane as depicted in Fig. 2a. Overall, migration follows a curved path, and at both SD, the migrating direction is along [111] pointing to/away-from V_{Ba}.

The band-decomposed charge densities depicted in Fig. 2b–e for those bands just beneath E_F. Again, they fall into gap states, indicating electron localization as expected for a small polaron. The extra electron in Ti^L occupies the Ti-3d_{xy} orbital, versus the Ti-3$d_z{}^2$ orbital with z|||[111] in Ti^{SD}. This abrupt change in the orbital character is caused by the drastically different local environments of Ti^L and Ti^{SD}. The relative energy lowering of the gap state, by 0.5 eV, estimated from the VBM-aligned pDOS for Ti^{SD} and Ti^L in Fig. 2f, is consistent with the corresponding changes in the ligand-field splitting in Fig. 2g.

As in the case of YSZ, a reduced Ti^{3+} cation has a higher mobility: its migration barrier (2.60 eV) is 0.93 eV lower than that of Ti^{4+} (3.53 eV). We believe a significant part of it again comes from the ligand field splitting of d orbitals of Ti^{SD}: in a trigonal planar ligand field, its short Ti-O bonds (~1.86 Å) significantly raise the energy levels of $3d_{x^2-y^2}$ and $3d_{xy}$ and lower the energy level of $3d_z{}^2$. In contrast, without any 3d electron, the HOMO of $Ti^{4+}$is always set at the VBM, so a migrating Ti^{4+} has no gap state and no energetic benefit to drawn on. Meanwhile, Fig. 2e illustrates that the extra electron at SD is oriented along the migrating direction (z = [111]) and completely avoids impinging the three nearest oxygens that define the "hard" directions. Therefore, the polaronium

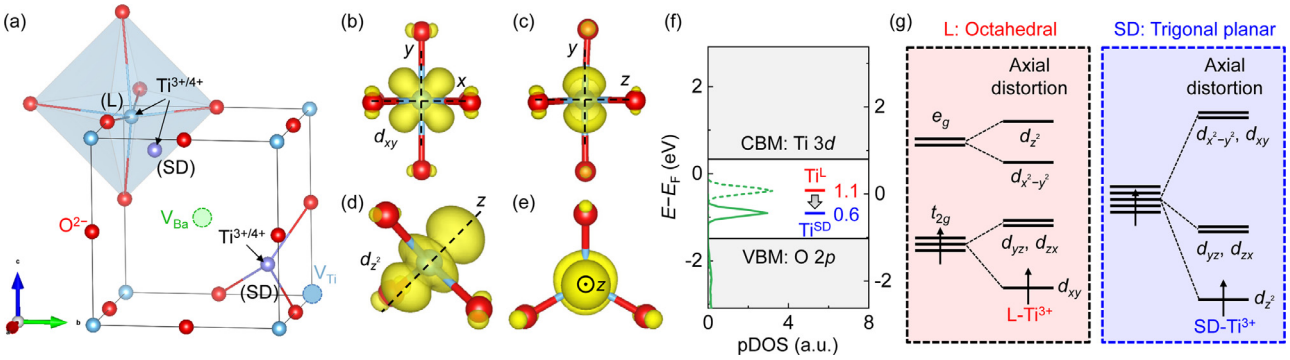

Fig. 2. **(a)** Schematic atomic structure for Ti ions at the ground state (L) and (two) saddle point states (SD) on the way to V_{Ti} by [110] migration in cubic $BaTiO_3$. Ti^{L} and V_{Ti} in blue, Ti^{SD} in purple, V_{Ba} in green, and O in red. **(b–e)** Band-decomposed charge densities of Ti^{3+} at L (b) and SD (d). (c) shows side view of (b), both with z||[001]. (e) shows side view of (d), both with z||[111]. One band is included, and the iso-surface is plotted with a charge density of 0.006 electron/Bohr^3. **(f)** Corresponding occupied pDOS below E_F of migrating Ti^{3+} at L (dotted curve) and SD (solid curve). Energy in eV relative to E_F is given by the left y-axis for L and the right y-axis for SD. Short bars indicate peak L and SD energy levels in eV relative to VBM. **(g)** Schematic ligand field splitting of Ti 3d orbitals at L (octahedral symmetry with axial distortion) and SD (trigonal planar symmetry with axial distortion). Ti^{SD} is coordinated by three short Ti^{SD}-O bonds (1.86 Å for all three), while other O are much further away. Therefore, the assignment of a trigonal planar field is justified. Band-decomposed charge densities of Ti^{3+} in (d, e) are consistent with the shape of d_z^2, which confirms the trigonal planar field splitting. (For interpretation of the references to colour in this figure legend, the reader is referred to the web version of this article.)

mechanism once again reigns in the migration of a reduced Ti^{3+} benefitting from the d character of the extra electron and the large anisotropic local distortion at SD, which not only lower the gap-state energy but also obviate the size effect. (For 6-fold coordination, the Shannon radii are $r_{Ti}{}^{4+}$=60.5 pm and $r_{Ti}{}^{3+}$=67 pm [26]).

5. Saddle point polaronium

Before proceeding to other examples of redox-enhanced ion migration, we pause to highlight and rationalize the salient features of the SD polaronium. As we already saw, the extra electron is "stuck' to the migrating cation despite the unfavorable prospect of forcing an oversized polaronium through a presumably narrow SD passage. While the symmetry-breaking SD environment is instrumental in lowering the energy and obviating the size effect of the extra electron, it is not clear why the electron is so "sticky" and why the accommodating environment is so readily provided. These environments do vary: in ZrO_2, the extra electron takes the d_{xy} orbital which reflects a soft x-y plane and a hard z direction; in $BaTiO_3$, the electron takes the $d_z{}^2$ orbital which reflects a soft z direction and a hard x-y plane. Below, we will provide a quantum mechanical picture to explain these features.

Following Mott and Stoneham [27], we envision a small polaron as a "molecular polaron" stabilized by a strong short-range electron-phonon interaction. In this simplified picture, a molecular polaron with a local atomic-displacement/bond-distortion q has three energy components depicted in Fig. 3. (a) A (positive) quantum-mechanical kinetic energy of a localized electron that cancels out, at $q<q_0$, (b) a (negative) electron-phonon interaction of a strength A, thus leaving a net non-zero $(a + b)$ energy of $-A(q-q_0)$ at $q>q_0$, and (c) a (positive) deformation energy $½\ kq^2$ against q, which is stored in the surrounding space of an elastic stiffness k. The total energy $(a + b + c)$ reaches a minimum $-A(A/2k-q_0)$ at $q^*=A/k$, which becomes a global minimum if $A/k>2q_0$. There is also an energy barrier, $½kq_0{}^2$ at $q = q_0$, before reaching this minimum. These considerations dictate whether a molecular polaron forms or not.

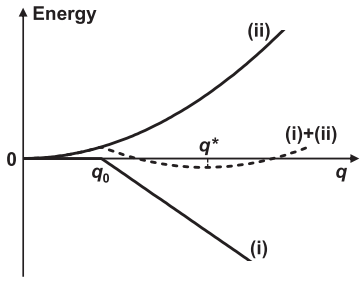

Fig. 3. Schematic energy diagram of molecular polaron after Mott and Stoneham [27]. Plotted against local atomic displacement and/or bond-distortion q are (i) sum of electron's kinetic energy and short-range interaction, which cancel each other at $q<q_0$, and (ii) deformation energy stored in the surrounding environment with an elastic stiffness k. Total energy has a global minimum at $q = q^*$ if $q^*>2q_0$.

Although the Mott-Stoneham picture portrays a static environment, the critical condition is also sensitive to the effective mass m^* of electron or hole through the kinetic energy $h^2/2m^*q_0{}^2$. Setting $h^2/2m^*q_0{}^2 - Aq_0$=0 at the truncation distance, we obtain $q_0=(h^2/2m^*A)^{1/3}$. Thus, the critical condition $A/k>2q_0$ reduces to $A^{4/3}m^{*1/3}/kh^{2/3}>2^{2/3}$, and the energy barrier becomes $kh^{4/3}/2^{5/3}m^{*2/3}A^{2/3}$. Therefore, in a polar material the most favorable locations for an extra electron or hole to form a small polaron are ones with a locally large A (e.g., at a Jahn-Teller cation in high-symmetry systems, see below), a locally small k (e.g., at a soft spot in an amorphous solid [28,29]), and a locally large m^* (e.g., at a gap state, where a narrow bandwidth Δ portends a large $m^*\sim\Delta^{-1}$.)

The above finding can explain why in YSZ and $BaTiO_3$ the small-polaron is stuck with the cation throughout the course of polaronium migration, and why their SD environments are synergistically deformed to best accommodate the polaronium. To see this, we first note that a short-range electron-phonon interaction with a large A is evident from the ligan-field splitting in Fig. 1g for Zr^{3+} and Fig. 2g for Ti^{3+}. In high-symmetry systems, such splitting is known as the Jahn-Teller effect, which breaks symmetry because a particularly strong short-range electron-phonon interaction demands that: if only one electron is present, then its energy degeneracy will be lifted by a spontaneous symmetry-breaking local distortion, thus allowing the electron to occupy a lower energy state hence lowering the system energy. Clearly, the energy splitting must be large enough to compensate for the energy penalty of poorer electrostatic shielding (evidenced by the Bader charge in Table 1) and the large strains that come with the distortion. This condition is more easily met at the SD that has an imaginary phonon frequency and a negative local stiffness k, which indicates that a restorative elastic force is no longer available and a static q^{SD} involving the poloronium and the local environment must result. This negative k will also allow the q^{SD} to orient in such a way to best suit the migrating polaronium and to maximize electrostatic

screening. Lastly, as illustrated in Figs. 1f and 2f, the SD in both YSZ and $BaTiO_3$ corresponds to an electronic gap state, which has a very narrow bandwidth hence a very large m^*. The above considerations that are valid for Zr^{3+} in YSZ and Ti^{3+} in $BaTiO_3$ all favor the formation of a small polaron: with only one d electron and a relatively large bandgap (4.5 eV in YSZ and 3.4 eV in $BaTiO_3$), they can take advantage of the softness of the SD environment to operate the polaronium mechanism, by tagging a gap-state polaronic electron to a migrating cation while obviating the size effect.

On the size effect, we already mentioned several times that the extreme anisotropy of the SD extra-d-electron distribution is beneficial. This can be further understood by recalling that there is a correspondingly extreme anisotropy of m^*. Specifically, along the soft direction(s) (x and y in YSZ and z in $BaTiO_3$), the more extended distribution implies a smaller tensorial component of m^*, thus a higher electron mobility. Conversely, along the hard direction(s) (z in YSZ and x and y in $BaTiO_3$ at SD), the more localized distribution implies a larger tensorial component of m^*, which does not matter because they are not the migration direction.

6. Reduced Ce and Ti cation migration with delocalized electron

As the bandgap decreases, distortion-enabled hybridization with O-2p and additional cation d or f orbitals becomes more important, which causes the gap state of the extra electron to spread and split. It may even cross over to the valence band or conduction band. Two cases are distinguished here. (a) If the spread of the SD state reaches the valence band, then the extra electron becomes a bonding electron, since only a hole state just beneath the VBM is itinerary in the valence band. (b) If the spread of the L state reaches the conduction band, then the extra electron becomes a large polaron. When this large polaron approaches a lattice defect, it will suffer some absorption by resonance scattering but the remaining electron wave will be scattered away. Physically, absorption of an initially itinerary large polaron means that it is temporarily localized at the defect site, forming a transitory polaronium. If this state lasts long enough, or equivalently if the probability of a transitory capture of a large polaron is more than that of a successful hopping event—which is extremely rare, then the state will participate in polaronium migration. In such case, a ground-state ion can "afford" to wait until it captures a polaron, then attempt a polaronium migration in an atomic vibration period that lasts about 0.1–1 ps, after that the polaron is released again. Since the absorption cross section increases with fluctuation, an accurate calculation for (b) must use a very large supercell to allow enough disorder. Therefore, our small-supercell studies described below may not capture the existence of a large polaron or to describe its dynamics accurately. Nevertheless, we will find that, for both (a) and (b), our calculations still yield an enhanced mobility for a reduced cation.

Our first example is CeO_2 and is summarized in Fig. 4 for Ce (Ce^{3+}: [Xe]$4f^1$ or Ce^{4+}: [Xe]$4f^0$) cation migration. Here the L state (Fig. 4b) is a small polaron manifest as a gap state, but the SD state (Fig. 4c) has crossed over to the valence band. (The small polaron L state is perhaps not an artifact of our small supercell, because small polaron conduction in oxides were reported in Nb-doped CeO_2 [30] and reduced CeO_2 [31]). Like the case of YSZ, with which CeO_2 shares the same structure, Ce^L and Ce^{SD} adopt CeO_7 and CeO_5 configurations, respectively, when a V_O is included in the supercell in Fig. 4a. Focusing on [110] migration of a reduced Ce^{3+}, we first view the band-decomposed charge densities just beneath E_F in Fig. 4b and c: they occupy a f_{xyz} or $f_{z(x^2-y^2)}$ orbital of Ce^L with z||[110]. This orbital is a gap state according to the pDOS (dash line in Fig. 4d). Turning to Ce^{SD}, Fig. 4c again reveals it is surrounded by a f_{xyz} or $f_{z(x^2-y^2)}$ orbital, but the orbital has rotated away from the previous position as it now has z||[001]. Interestingly, although the extra electron still hovers around Ce^{SD} and the polaronium is intact, its f-orbital energy is so low that it now lies below the VBM (solid line in Fig. 4d), signaling a possible benefit from f-p hybridization. This is confirmed in Fig. 4c by π bonding within CeO_5 between Ce-4f and O-2p as well as some spillover σ/π hybridization with O-2p of oxygens further beyond, and the propagation of hybridization is strongly anisotropic apparently because of the symmetry-breaking local distortion around Ce^{SD}. Compared to Zr^{SD} that also sees π bonding between Zr-4d and O-2p within ZrO_5 but no spillover hybridization further beyond (Fig. 1b), Ce's stronger hybridization is reasonable because its bandgap is smaller and its 4f orbitals are more extended than Zr's 4d orbitals. Clearly, unlike Ce^{3+}, Ce^{4+} without an extra electron cannot benefit from the strong and anisotropic hybridization and the attendant lowering of electronic energy. This explains why the migration barrier of Ce^{3+} (3.28 eV) in Table 1 despite its bigger size is 0.68 eV lower than that of Ce^{4+} (3.96 eV). (For 6-fold coordination, the Shannon radii are $r_{Ce}{}^{4+}$=87 pm and $r_{Ce}{}^{3+}$=101 pm [26]).

Our second example revisits Ti migration in $BaTiO_3$, this time with a V_O instead of V_{Ba} in the supercell, as summarized in Fig. 5. For the extra electron here, it proves to be a case of a transition from a L-state conduction electron in the conduction band to a SD-state bonding electron in the valence band. Taking advantage of the neighboring V_O, the Ti cation now migrates in the [001] direction in Fig. 5a. The extra electron in the L state is mostly in the conduc-

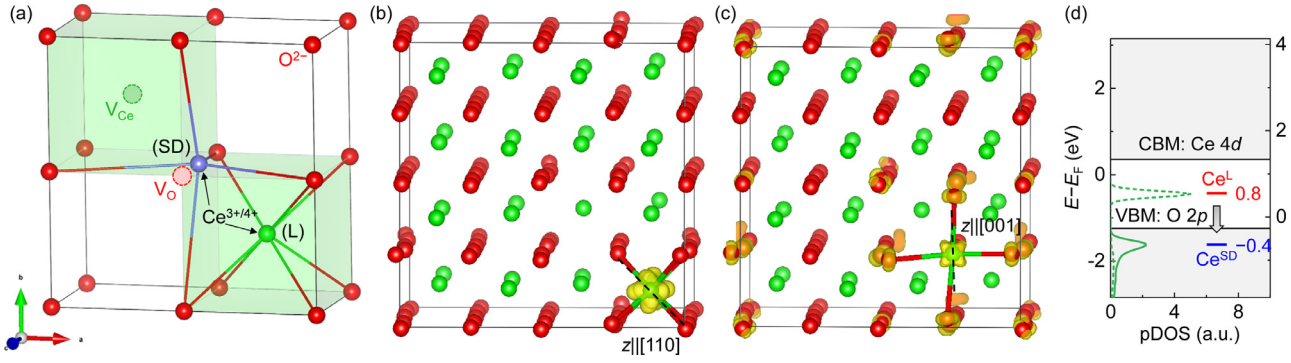

Fig. 4. **(a)** Schematic atomic structure for Ce ions at the ground state (L) and the saddle point state (SD) in CeO_2. Ce^L and V_{Ti} in green, Ce^{SD} in purple, and O and V_O in red. **(b, c)** Band-decomposed charge densities of Ce^{3+} at L (b) and SD (c). One band is included in (b) and two bands are included in (c), and the iso-surface is plotted with a charge density of 0.018 electron/Bohr^3. **(d)** Corresponding occupied pDOS below E_F of migrating Ce^{3+} at L (dotted curve) and SD (solid curve). Energy in eV relative to E_F is given by the left y-axis for L and the right y-axis for SD. Short bars indicate peak L and SD energy levels in eV relative to VBM. (For interpretation of the references to colour in this figure legend, the reader is referred to the web version of this article.)

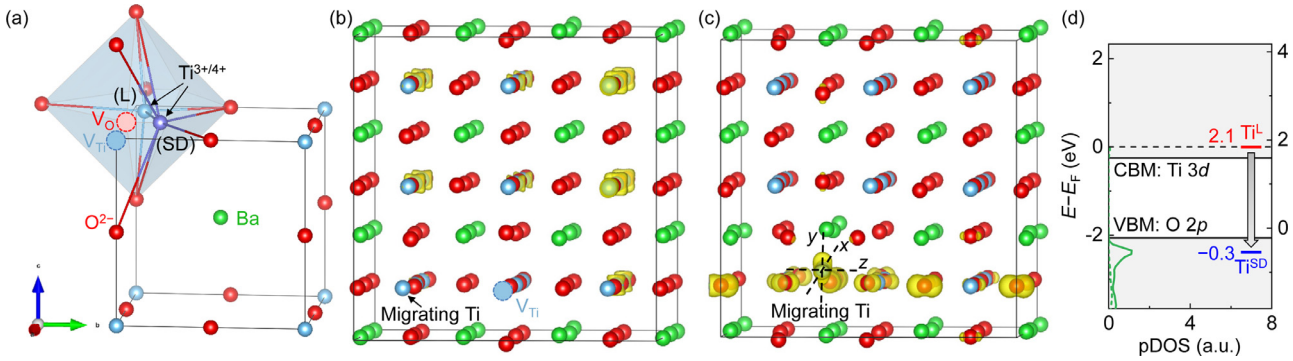

Fig. 5. **(a)** Schematic atomic structure for Ti ions at the ground state (L) and the saddle point state (SD) in cubic $BaTiO_3$ for [100] migration. Ti^L and V_{Ti} in blue, Ti^{SD} in purple, V_{Ba} in green, and O and V_O in red. **(b, c)** Band-decomposed charge densities of Ti^{3+} at L (b) and SD (c). One band is included in (b), four bands are included in (c), and the iso-surface is plotted with a charge density of 0.024 electron/Bohr^3. **(d)** Corresponding occupied pDOS below E_F of migrating Ti^{3+} at L (dotted curve) and SD (solid curve). Energy in eV relative to E_F is given by the left *y*-axis for L and the right *y*-axis for SD. Short bars indicate peak L and SD energy levels in eV relative to VBM. (For interpretation of the references to colour in this figure legend, the reader is referred to the web version of this article.)

tion band (Fig. 5d), suggesting a possible large polaron. Previous first-principles calculations also found a V_O alone cannot stabilize a small polaron, and an off-centered Ti simulated by a hybrid first-principles-Monte-Carlo method implemented in a large supercell can [32]. Experimentally, while small polarons apparently participate in DC conduction as well as local hopping around defects in $BaTiO_3$, in closely related cubic $SrTiO_3$ that has no Ti distortion, there is a transition of DC conductivity from large polaron conduction at low temperature to small polaron conduction at high temperature. Thus, disorder is important for polaron localization in titanates, as well as in other perovskite and related structures [33,34]. (More disorder can be provided by other defects, for example by V_{Ba} around which we did find a gap state in Fig. 2f. This is reasonable because, compared to a V_O, an *A*-site vacancy is energetically more costly as it comes with more lattice distortions. In fact, a *B*-site vacancy will introduce even more distortions, which is why it is rare in perovskite oxides.) In contrast, the extra electron of Ti^{SD} is a bonding electron as it has crossed over to the valence band as shown by the solid line in Fig. 5d. With this electron-energy transition across the band gap from a Ti^L to Ti^{SD}, one may expect such electronic-energy lowering would lower the migration barrier of Ti^{3+}. This is verified in Table 1: the migration barrier of Ti^{3+} (6.63 eV) is 1.22 eV less than that of Ti^{4+} (7.75 eV).

The absence of electron localization at Ti^L is further confirmed by Fig. 5b showing, around the (to-be-migrating) Ti, little band-decomposed charge densities just beneath E_F. However, there is a SD polaronium since the extra electron now hovers around Ti^{SD} with an orbital character of a distorted d_{xy} in Fig. 5c, suggesting a local environment of a distorted octahedron. Note that if site symmetry were followed, then Ti^{SD} should have coincided with V_O situating at the center of two intersecting (100) O_4 planes, i.e., it should have formed a (tetragonal) TiO_8 polyhedron. Therefore, there must be a strong enough short-range electron-phonon interaction that forces an off-center Ti^{SD} movement, along [010] as shown in Fig. 5a, thus resulting in a distorted TiO_6 octahedron with two short Ti-O bonds. Moreover, Fig. 5c reveals that the d_{xy} orbital further triggers (i) π-bonding with the O-2*p* orbitals in one O_4 plane and (ii) O-2*p*/O-2*p* σ-bonding between the nearest neighbor O in the O_4 plane and the O further beyond. We interpret such "chain reaction" of *d*-*p* and *p*-*p* hybridization set off by the strong short-range electron-phonon interaction as the mechanism that enables the extra electron to insert itself into a bonding electron state well below the VBM (solid line in Fig. 5d). Before the extra electron is inserted, the bonding electron state is like an infinite chain of hybridized O-2*p*/O-2*p* bonds between neighboring O. The extra electron pushes out the wavefunction of one bonding electron state and replaces it in a very similar form and with a very similar energy, which is what the band-decomposed charge densities in Fig. 5c show.

7. Oxidized O anion in battery cathodes

If the broad analogy to the Jahn-Teller effect holds, then Fig. 6 suggesting an overall energy lowering by way of a spontaneous local distortion can happen to not only all the reduced d^1/f^1-cations (benefiting from an electron occupying a lower energy level) but also oxidized p^5-anions (benefiting from a missing electron away from a higher energy level). If so, in a polaronic material, O^- should have a lower migration barrier than O^{2-}.

Oxidation of O^{2-} to O^- in high-voltage oxide cathodes is an active current research area of lithium-ion battery because of its potential to deliver a higher capacity from light oxygen instead of heavy transition metals [6,7,35–37]. However, extreme oxidation is sometimes accompanied by microstructure and phase instabil-

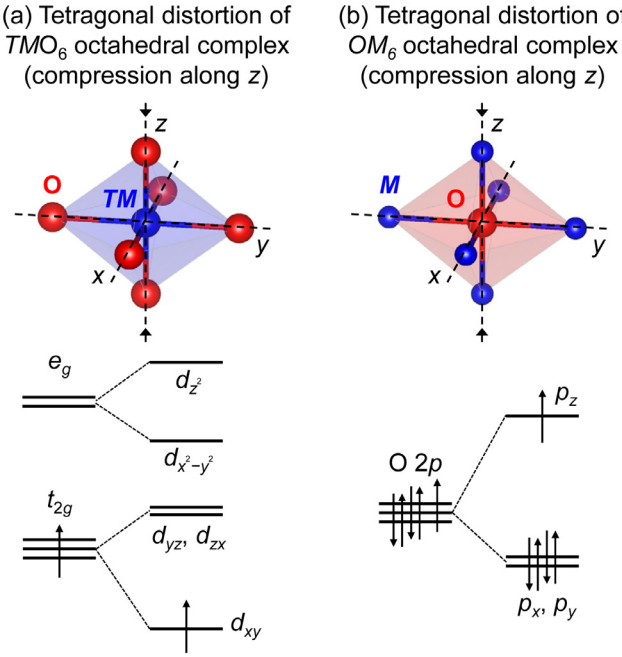

Fig. 6. **(a)** Ligand field splitting of *d* orbitals of TMO_6 octahedral complex with tetragonal distortion by compression along *z*. *TM* denotes a transition metal ion with d^1 electron configuration. **(b)** Ligand field splitting of O-2*p* orbitals of OM_6 octahedral complex with tetragonal distortion by compression along *z*. O denotes an oxygen ion O^- with $2s^22p^5$ electron (i.e., one hole) configuration. *M* denotes a cation.

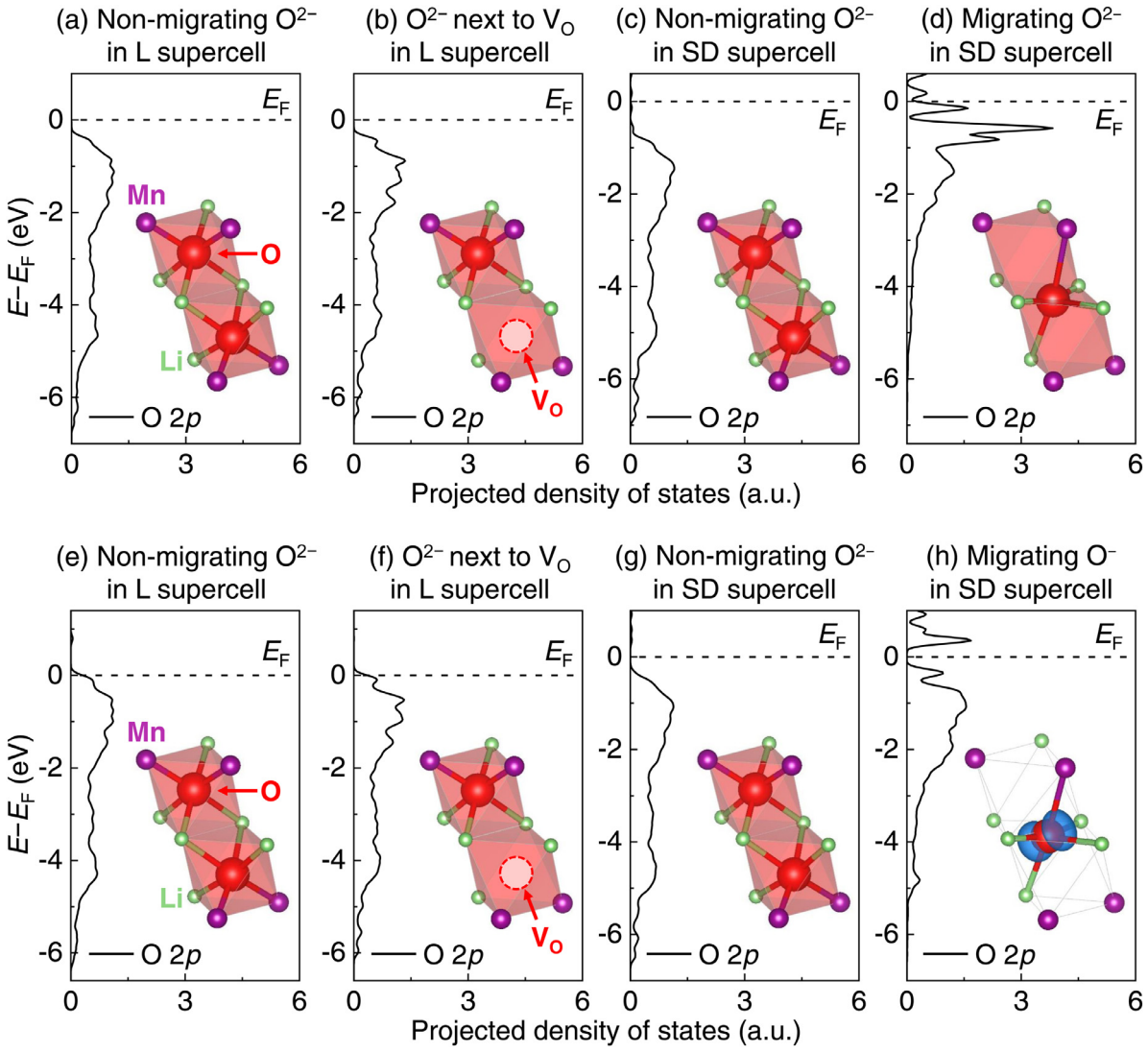

Fig. 7. pDOS of oxygen ion in ground state and saddle point in two cases: without an extra hole in supercell (**a-d**) in upper panel and with an extra hole in supercell (**e–h**) in lower panel. Ground state (L) supercell: **(a, e)** average non-migrating O^{2-} and **(b, f)** to-be-migrating O^{2-} (next to V_O), both from the same calculation in the same supercell. Saddle point (SD) supercell: **(c, g)** average non-migrating O^{2-} and **(d, h)** migrating O^{2-}, both from the same calculation in the same supercell. Insets of (a–h): schematic local structures. Inset of (h): the electron cloud in blue denotes unoccupied states (i.e., hole states) with iso-charge-density of 0.006 electron/Bohr^3. Since (h) has a localized hole, its oxygen is actually O^-. See text for the calculation of pDOS of average non-migrating O^{2-}. (For interpretation of the references to colour in this figure legend, the reader is referred to the web version of this article.)

ity, suggesting an enhanced O^- mobility may play a role [6,38]. Compared to O^{2-}, a migrating O^- like a reduced cation should encounter less electrostatic interaction. But it has an advantage over reduced cation because of its smaller size, which could make O^- migration even easier. The expectation is confirmed by the following study of O migration in $Li_{4/3}Mn_{2/3}O_2$ (Mn = Mn^{4+}), which has alternating cation layers of Li and $Li_{1/3}Mn_{2/3}$ separated by anion layers of O, stacked like an ordered NaCl structure. This compound is chosen for comparative study not only because it is a model system of high-voltage oxide cathodes in Li-ion batteries but also because its vacancy exchange of O, like vacancy exchange of (highest-valence) cation—Zr in ZrO_2, Ce in CeO_2, and Ti in $BaTiO_3$, is the slowest step in mass transport.

Necessitated by the complexity of the problem, several different study methods were used. First, we note that the relevant experimental studies were all on alloyed compounds containing other transition metal cations more easily oxidizable than Mn^{4+}. But they cannot be readily modeled in a practically sized supercell because the alloying cations also break local symmetry, which will favor polaron formation making it difficult to isolate the effect of oxygen oxidation. (Indeed, oxygen hole polaron has been reported in such alloyed compounds [35,36]). Second, the complex energy landscape with active oxygen redox leads us to use the dimer method [21], which provides a faster convergence than the climbing-image NEB method. We first examine the L-state supercell after identifying the migrating O, we next zoom in at the site of the migrating O and at another site far from it (to be called non-migrating oxygen) to compare their pDOS against the same E_F; the procedure is repeated for the SD supercell to obtain another comparison. To provide a representative picture of all the non-migrating oxygens, we first exclude the O-2*p* states of the migrating O from the sum of all the 2*p* states in the supercell, then average the remaining 2*p* states and regard it as an "average non-migrating oxygen". With these methods, we can obtain all the pertinent data as before for both the unoxidized state and the oxidated state, the latter created by removing an electron from the supercell.

The outcome proves remarkably simple. The pDOS of O-2*p* electrons in Fig. 7a–d (non-migrating O^{2-} and migrating O^{2-}— both L and SD state, without an extra hole added to the supercell) and

Fig. 7e–h (non-migrating O^{2-} and migrating O^{-}—both L and SD state, with an extra hole added to the supercell) are all similar except in one case. The exception concerns O^{SD}, shown in Fig. 7d for unoxidized oxygen O^{2-} and Fig. 7h for oxidized oxygen O^{-}, which has a dramatically increased spectrum weight at the high-energy end of the pDOS. The increase is accompanied by the emergence of several sharp peaks reminiscent of orbitals in a heavily distorted local environment. This makes sense judging from the following observations. (i) As depicted in the insets, O^{SD} has a less symmetric and poorer screened OLi_5Mn (cation charge = 9; or OLi_4Mn if a shorter cutoff bond length is used) environment compared to the OLi_4Mn_2 (cation charge = 13) environment of O^{L}. (ii) O^{SD} has a bond valence sum of 1.3, which is significantly smaller than the formal charge of O^{2-} and the sum of 2.0–2.1 for O^{L}. (Parameters used for the calculation are: R_0=1.466 and b = 0.37 for Li^{+}-O^{2-}, and R_0=1.753 and b = 0.37 for Mn^{4+}-O^{2-}.) (iii) O^{SD} has less Mn-3d/O-2p hybridization. These observations all indicate inadequate electropositive screening around O^{SD}, which calls for a hole polaron to form, which is confirmed by the band decomposed charge densities in the inset of Fig. 7h showing an O-2p hole state at O^{SD}. With this hole, the oxidized O^{-} can empty the high-energy pDOS very close to E_F thus realizing a significant energy saving. The value of the Bader charge in Table 1 is consistent with this picture: it stays between 7.35 and 7.41 at all time except for the oxidized O^{SD} when it falls to 7.05, again signaling the formation of a hole polaron. Meanwhile, confirming our expectation, the migration energy is lowered from 3 eV for O^{2-} to 2.33 eV for O^{-} as shown in Table 1. Further calculations including the effect of one or more V_{Li} and massive oxygen redox, which facilitates O migration, upheld the above conclusion [39].

We note that the hole state in Fig. 7h is disposed perpendicular to the migration direction and points to neither Li nor Mn. According to Fig. 6b, the saddle-point compression in the transverse direction leaves a 2-p_z hole in addition to a 2-p_z electron, which explains the perpendicular disposition above. Since the single 2-p_z electron is expected to maximize bonding with the surrounding cations, it will push away the non-bonding 2-p_z hole, which explains why the hole state in Fig. 7h does not point to any cation. Nevertheless, the figure gives evidence that while the p-orbitals are less anisotropic and localized as the d/f-orbitals, they still advantageously orient themselves in the SD state to maximize bonding and minimize repulsion.

8. Experimental evidence

We now turn to the experimental evidence. First, we note that there are many reports of enhanced M^{4+} diffusion in fluorite-structured zirconia, ceria and perovskite titanates under reducing conditions at high temperatures (>1000 °C) rendered by either a reducing atmosphere or cathodic charging [1,2,24,40,41]. (Additional references are provided in Ref. [42]). One legitimate question, though, is whether this is but a special case of a general trend of faster M^{3+} than M^{4+} because of a lower electrostatic repulsion against M^{3+} migration. If so, then finding it in reduced oxides is merely fortuitous and unrelated to small polarons. (The electrostatic advantage, though, is countered by the difficulty of a larger M^{3+} to migrate. Here, we refer to M^{3+}that has a d^0 or f^7 configuration, such as $Y^{3+}$and Gd^{3+} below.) But if so, then Y^{3+} should diffuse faster than Zr^{4+} in $Zr_{1-x}Y_xO_{2-x/2}$, and Gd^{3+} should diffuse faster than Ce^{4+} in $Ce_{1-x}Gd_xO_{2-x/2}$. This was not found in either material according to the electrical de-mixing and tracer diffusion experiments, which report similar Y^{3+} and Zr^{4+} diffusivity [43–45]. In contrast, there are many reports of hugely enhanced grain growth and other kinetic processes—all of them controlled by the majority cation species, Zr and Ce in these and other similar materials—in reduced $Zr_{1-x}Y_xO_{2-x/2}$, $Ce_{1-x}Gd_xO_{2-x/2}$ and other Zr^{3+}/Ce^{3+}-containing zirconia and ceria ceramics.

In general, in these ceramics, M^{4+} (M=Zr or Ce) diffusion assisted by oxygen vacancies should prevail under an oxidizing condition, and M^{3+} (M=Zr or Ce) diffusion assisted by oxygen vacancies should prevail under a reducing condition. Without reduction, the cation diffusivity is proportional to $[M^{4+}][V_M]\exp(-(\text{Barrier of } M^{4+})/k_BT)$ with $[M^{4+}]$ set to be 1; with reduction, it is proportional to $[M^{3+}][V_M]\exp(-(\text{Barrier of } M^{3+})/k_BT)$ with $[M^{3+}]$ depending on the reduction level. Therefore, the enhancement factor due to reduction is $([M^{3+}]/[M^{4+}])\exp(\Delta E/k_BT)$, where ΔE is the reduction in the barrier height in **Table I** from M^{4+} to M^{3+}—both assisted by oxygen vacancies, which is 1.14/0.68 eV for ZrO_2/CeO_2. (Although the diffusion path varies depending on whether solute drag is important or not, which in turn varies with systems, here we assume the same ΔE applies to lattice migration and grain boundary migration, and to cubic and tetragonal polymorphs.) When reduction is severe, $[M^{3+}]/[M^{4+}]$ approaches 1, and the ΔE difference alone gives an enhancement factor of 7950 for zirconia and 210 for ceria at 1200 °C. This condition is experimentally met for (i) $Zr_{0.852}Y_{0.148}O_{1.926}$ (cubic YSZ) and $Zr_{0.942}Y_{0.058}O_{1.971}$ (tetragonal YSZ) under electro-reduction at 1200 °C, its grain boundary mobility is >1000 times faster than that in air [1,24], and (ii) $Ce_{0.9}Gd_{0.1}O_{1.95}$ in 5% H_2 at 1200 °C, its mobility is 400 times faster than that in air [1]. So, there is a reasonable agreement between the estimates and the experimental observations. Under less reducing conditions, the enhancement factor should be smaller because $[M^{3+}]/[M^{4+}]<<1$. $[M^{3+}]/[M^{4+}]$ can be estimated from the thermodynamic data of the reaction $O_O^{\times} = 2e + V_O^{\bullet\bullet} + \frac{1}{2}O_2$ by fixing $[V_O^{\bullet\bullet}]$ set by the acceptor dopants [46,47]. For $Zr_{0.852}Y_{0.148}O_{1.926}$/$Zr_{0.942}Y_{0.058}O_{1.971}$ at 1200 °C in an oxygen partial pressure of 10^{-10} atm (which is representative for 5% H_2), we estimate $[M^{3+}]/[M^{4+}]$ of 1.7×10^{-4}; small enhancement factors of 1.5–2 for their grain boundary mobilities in 5% H_2 over those in air were indeed observed [1]. Likewise, CeO_2 in air has a $[M^{3+}]/[M^{4+}]\sim10^{-3}$ at 1300 °C, which explains why its grain boundary mobility is only 2 times faster than that in oxygen [48]. The different outcomes why Y^{3+} and Gd^{3+} do not have a much higher diffusivity than Zr^{4+} and Ce^{4+} despite their lower charge (though a larger size) can also be explained in terms of cation's electronic configuration and the polaronium mechanism, which is expected for Zr^{3+} ($4d^1$) and Ce^{3+} ($4f^1$) but not Y^{3+} ($4d^0$) and Gd^{3+} ($4f^7$).

Of the above, Ce is particularly interesting since Ce^{4+}/Ce^{3+} conversion readily occurs at ambient conditions as reflected in the light-yellow color of CeO_2, and a small amount of Ce^{3+}should be enough to provide all the electrons needed for polaron localization at the saddle points. This is because, as mentioned before, only very few saddle points witness cation migration at any given moment given the very low probability of ion migration events, and with that an electron initially attracted to one saddle point to aid a successful migration event there can be later recycled to another saddle point and aid another migration event again. Indeed, as we documented in Ref. [42], there are many examples in support of the above expectation: a small presence of Ce can affect a systematic change in grain size, even a dramatic transition in the microstructure [49]. Therefore, like a catalyst or a free radical that enhances chemical reactivity, a mixed-valence cation dopant such as Ce has a powerful effect on enhancing the mobility of host d^0/f^0 cations.

The experimental observations most relevant to Fig. 6b is O^{-} diffusion in Li-rich cathodes, e.g., $Li_{1.2}Ni_{0.13}Co_{0.13}Mn_{0.54}O_2$, which has a layered structure similar to $Li_{4/3}Mn_{2/3}O_2$ and an O local structure adopted in Fig. 6b. These cathodes are of interest to Li-ion batteries because they allow O^{2-}/O^{-} redox at high cathodic potentials, which delivers additional capacities not available in conventional cathodes that rely on transition metal redox only. How-

ever, during high-voltage charging cycles, they suffer from continuous oxygen loss, oxygen gas evolution, and lattice cavitation [6,7], which must involve O^{2-}/O^{-} diffusion from the bulk to the surface. As mentioned before, O^{2-} is the slowest diffusing ion in this class of compounds, so it is unlikely to diffuse at ambient temperature without some unexpected mechanism, which is identified here: by forming a complex of a small hole polaron and a saddle-point O^{2-}. With the polaronium mechanism and the same structure as in Fig. 6b (octahedral O by metal-ion ligands) but including massive Li vacancies, which is appropriate at high cathodic potentials, we calculated a migration energy of around 0.6 eV for O^{-} [39]. This is low enough to activate room-temperature migration of O, which explains the above observation.

An even more interesting case is the following example of the catalytic effect of acceptor dopants on enhancing O^{2-} mobility. Under a sustained DC voltage, perovskite titanates used in billions of multilayer capacitors suffer aging in their resistance, initially rising gradually and later falling precipitously [50]. This process is controlled by V_O redistribution that triggers the Ti^{4+}/Ti^{3+} redox reaction, which eventually leads to enhanced *p*-type conduction near the anode and enhanced *n*-type conduction near the cathode. When a small amount of Al^{3+} and Fe^{3+} is used to substitute Ti^{4+}, Al^{3+}-doped $SrTiO_3$ ages only modestly faster than undoped $SrTiO_3$ but Fe^{3+}-doped $SrTiO_3$ ages much faster [51]. This supports the hole polaronium mechanism, because while both Al^{3+} and Fe^{3+} can create V_O that aggravates aging, only mixed-valence $Fe^{2+}/Fe^{3+}/Fe^{4+}$ can provide holes that go around to help the migrating O^{2-} at the saddle points, i.e., creating a hole polaronium to greatly accelerate aging.

It is clear from the above examples that reducing/oxidizing atmospheres or, equivalently, cathodic/anodic charging can provide electrons/holes, as can a small amount of mixed-valence donor/acceptor dopants, and these are very potent effects because they are catalytic. In materials engineering, doping to control defect population, hence diffusivity, is already well known as defect chemistry. Our study has revealed an equally if not more important role of doping: it enhances defect (cation/anion vacancy) mobility by forming radical-like transition-state ions that migrate with a greatly reduced barrier, and like a free radical the extra electron/hole can be redeployed from one location to another to enhance ion mobility catalytically. This realization immediately resolves one long-standing conundrum in solid-state ionics that defect chemistry has failed to explain, namely why many reduced oxides enjoy higher diffusivity even though they must contain more oxygen vacancies that should have suppressed cation vacancies via the Schottky-pair reaction. We now see that, with the intervention of small polaron and polaronium, the adverse effect on defect population is overwhelmed by the beneficial effect on cation mobility. As discussed in Ref. [42], this is but one example of an extensive list of problems on zirconia, ceria, titanates and even alumina that are now understood by applying our mechanism. To take advantage of the mechanism, one should use dopants and compounds known to be susceptible to the Jahn-Teller-like effect.

Lastly, the transient polaronium mechanism may be relevant to several technologically important observations that have gone unexplained until now. (1) Enhanced sintering by a field ranging from a slow-varying DC voltage ("spark plasma" sintering [52] and "flash" sintering [3]) to a microwave [53], which may cause non-equilibrium redox reactions in the sample, thus creating electrons and holes that enhance ion mobility. (2) Valence-change (resistance) memory using oxide and other insulator thin films whose resistance changes upon the formation, rupture and reconnection of conducting filaments, which may be enabled by enhanced cation/anion diffusion because of non-equilibrium electrons and holes generated by the huge electrical field [4]. (Oxides of Ta^{5+}, Hf^{4+} and Ti^{4+}, all d^0 cations, are leading candidates for such memory, which is also being explored for neuromorphic computing.) (3) Superior plasticity of a severely reduced suboxide layer at the Zr/ZrO_2 interface [54,55], which help support the oxide scale above it and prevent oxidation of the metal beneath it, possibly because the suboxide has copious Zr^{3+} that diffuses much faster than Zr^{4+}. Similarly enhanced kinetics mediated by radical-like polaronium migration catalytically or even autocatalytically enabled by equilibrium or non-equilibrium small electron/hole polarons may also explain other dynamic observations in nominally insulating compounds in advanced applications, including those under extreme conditions such as irradiation in *in-situ* transmission electron microscopy and in nuclear reactors.

9. Conclusions

(1) A polaronium, defined as a transitory complex of a polaronic electron or hole and its migrating counterion, is a highly mobile species in ionic compounds where the host counterion is a d^0 or f^0 cation or a p^6 anion.
(2) The stability and enhanced mobility of a polaronium is due to the electron-phonon interaction that results in a Jahn-Teller effect causing local distortion and lowering the electronic energy around a defect, which has a low stiffness thus easily accommodates any required distortion. Such interaction is especially strong for d^1 and f^1 cations, obtained by reducing d^0 and f^0 cations. Likewise, it is especially strong for p^5 anions, obtained by oxidizing p^6 anions.
(3) Polaronium migration going from the ground state to the saddle point state is immune to the size effect because the *d*/*f*/*p*-orbitals can reorient to minimize repulsion.
(4) Once a migration event of a polaronium is completed, its polaronic electron/hole can be recycled elsewhere. Thus, very few electrons and holes are needed to enable the mechanism. In this sense, they behave like free radicals and catalysts, which are known to enhance chemical reactivity. Indeed, the polaronium itself is a radical-like ion that enjoys enhanced mobility.
(5) The polaronium mechanism can explain many observations of enhanced kinetics in (mixed-valence-cation) doped and redox ceramics that remain unexplained until now. It may also help understand how enhanced kinetics arise from non-equilibrium electrons/holes generated under dynamic or extreme thermal/field/irradiation conditions.

Declaration of Competing Interest

The authors declare that they have no known competing financial interests or personal relationships that could have appeared to influence the work reported in this paper.

Acknowledgments

Work by Y.D. was performed in partial fulfillment of the PhD requirements at the University of Pennsylvania for which Y.D. and I.W.C. acknowledge support by the Department of Energy (BES grant no. DEFG02-11ER46814) and the facility (LRSM) support by the U.S. National Science Foundation (grant no. DMR-1120901). Q.L. acknowledges support by the startup funding from University of Michigan. J.L. acknowledges support by a subcontract of the U.S. Department of Energy (USDOE), Office of Energy Efficiency and Renewable Energy (EERE), Advanced Manufacturing Office (AMO) R&D Projects Emerging Research Exploration, under DOE Idaho Operations Office with contract no. DE-AC07-05ID14517.

References

[1] Y. Dong, H. Wang, I.W. Chen, Electrical and hydron reduction enhances kinetics in doped zirconia and ceria: I, grain growth study, J. Am. Ceram. Soc. 100 (2017) 876–886.
[2] Y. Dong, I.W. Chen, Electrical and hydrogen reduction enhances kinetics in doped zirconia and ceria: II. Mapping electrode polarization and vacancy condensation in YSZ, J. Am. Ceram. Soc. 101 (2018) 1058–1073.
[3] M. Cologna, B. Rashkova, R. Raj, Flash sintering of nanograin zirconia in <5 s at 850°C, J. Am. Ceram. Soc. 93 (2010) 3556–3559.
[4] A. Wedig, M. Luebben, D.Y. Cho, M. Moors, K. Skaja, V. Rana, T. Hasegawa, K.K. Adepalli, B. Yildiz, R. Waser, I. Valov, Nanoscale cation motion in TaOx, HfOx and TiOx, memristive systems, Nat. Nanotechnol. 11 (2016) 67–74.
[5] G.Y. Kim, A. Senocrate, T.Y. Yang, G. Gregori, M. Gratzel, J. Maier, Large tunable photoeffect on ion conduction in halide perovskites and implications for photodecomposition, Nat. Mater. 17 (2018) 445–449.
[6] Z. Zhu, D. Yu, Y. Yang, C. Su, Y. Huang, Y. Dong, I. Waluyo, B. Wang, A. Hunt, X. Yao, J. Lee, W. Xue, J. Li, Gradient Li-rich oxide cathode particles immunized against oxygen release by a molten salt treatment, Nat. Energy 4 (2019) 1049–1058.
[7] P. Yan, J. Zheng, Z.K. Tang, A. Devaraj, G. Chen, K. Amine, J.G. Zhang, L.M. Liu, C. Wang, Injection of oxygen vacancies in the bulk lattice of layered cathodes, Nat. Nanotechnol. 14 (2019) 602–608.
[8] D. Emin, Polarons, Cambridge University Press, 2013.
[9] G. Kresse, D. Joubert, From ultrasoft pseudopotentials to the projector augmented-wave method, Phys. Rev. B 59 (1999) 1174–1758.
[10] J.P. Perdew, K. Burke, M. Ernzerhof, Generalized gradient approximation made simple, Phys. Rev. Lett. 77 (1996) 3865–3868.
[11] G. Kresse, J. Furthmuller, Efficiency of ab-initio total energy calculations for metals and semiconductors using a plane-wave basis set, Comp. Mater. Sci. 6 (1996) 15–50.
[12] S.L. Dudarev, G.A. Botton, S.Y. Savrasov, C.J. Humphreys, A.P. Sutton, Electron-energy-loss spectra and the structural stability of nickel oxide: an LSDA+U study, Phys. Rev. B 57 (1998) 1505–1509.
[13] A.R. Puigdollers, F. Illas, G. Pacchioni, Effect of nanostructuring on the reactivity of zirconia: a DFT+U study of Au atom adsorption, J. Phys. Chem. C 120 (2016) 17604–17612.
[14] M. Nolan, J.E. Fearon, G.W. Watson, Oxygen vacancy formation and migration in ceria, Solid State Ionics 177 (2006) 3069–3074.
[15] J.J. Brown, Z. Ke, W. Geng, A.J. Page, Oxygen vacancy defect migration in titanate perovskite surfaces: effect of the a-site cations, J. Phys. Chem. C 122 (2018) 14590–14597.
[16] A. Jain, G. Hautier, S.P. Ong, C.J. Moore, C.C. Fischer, K.A. Persson, G. Ceder, Formation enthalpies by mixing GGA and GGA + *U* calculations, Phys. Rev. B 84 (2011) 045115.
[17] Y. Dong, L. Qi, J. Li, I.W. Chen, A computational study of yttria-stabilized zirconia: II. Cation diffusion, Acta Mater. 126 (2017) 438–450.
[18] T. Zacherle, A. Schriever, R.A. De Souza, M. Martin, *Ab initio* analysis of the defect structure of ceria, Phys. Rev. B 87 (2013) 134104.
[19] G.V. Lewis, C.R.A. Catlow, Computer modelling of barium titanate, Radiat. Eff. 73 (1983) 307–314.
[20] G. Henkelman, B.P. Uberuaga, H.A. Jonsson, A climbing image nudged elastic band method for finding saddle points and minimum energy paths, J. Chem. Phys. 113 (2000) 9901–9904.
[21] P. Xiao, D. Sheppard, J. Rogal, G. Henkelman, Solid-state dimer method for calculating solid-solid phase transitions, J. Chem. Phys. 140 (2014) 174104.
[22] W. Tang, E. Sanville, G. Henkelman, A grid-based Bader analysis algorithm without lattice bias, J. Phys. Condens. Matter 21 (2009) 084204.
[23] K. Momma, F. Izumi, *VESTA 3* for three-dimensional visualization of crystal, volumetric and morphology data, J. Appl. Crystallogr. 44 (2011) 1272–1276.
[24] S.W. Kim, S.G. Kim, J.I. Jung, S.J.L. Kang, I.W. Chen, Enhanced grain boundary mobility in yttria-stabilized cubic zirconia under an electric current, J. Am. Ceram. Soc. 94 (2011) 4231–4238.
[25] T. Mizoguchi, N. Takahashi, H.S. Lee, First-principles study on migration mechanism in $SrTiO_3$, Appl. Phys. Lett. 98 (2011) 091909.
[26] R.D. Shannon, Revised effective ionic radii and systematic studies of interatomic distances in halides and chalcogenides, Acta Cryst. A32 (1976) 751–767.
[27] N.F. Mott, A.M. Stoneham, The lifetime of electrons, holes and excitons before self-trapping, J. Phys. C Solid State Phys. 10 (1977) 3391–3398.
[28] X. Yang, I. Tudosa, B.J. Choi, A.B.K. Chen, I.W. Chen, Resolving voltage-time dilemma using an atomic-scale lever of subpicosecond electron-phonon interaction, Nano Lett. 14 (2014) 5058–5067.
[29] Y. Lu, A. Alvarez, C.H. Kao, J.S. Bow, S.Y. Chen, I.W. Chen, An electronic silicon-based memristor with a high switching uniformity, Nat. Electron. 2 (2019) 66–74.
[30] I.K. Naik, T.Y. Tien, Electrical conduction in Nb_2O_5-doped cerium dioxide, J. Electrochem. Soc. 126 (1979) 562–566.
[31] H.L. Tuller, A.S. Nowick, Small polaron electron transport in reduced CeO_2 single crystals, J. Phys. Chem. Solid 38 (1977) 859–867.
[32] N. Tsunoda, Y. Kumagai, F. Oba, Stabilization of small polarons in $BaTiO_3$ by local distortions, Phys. Rev. Mater. 3 (2019) 114602.
[33] M. Alaydrus, I. Hamada, Y. Morikawa, Mechanistic insight into oxygen vacancy migration in $SrFeO_{3-\delta}$ from DFT+*U* simulations, Phys. Chem. Chem. Phys. 23 (2021) 18628.
[34] T. Das, J.D. Nicholas, Y. Qi, Polaron size and shape effects on oxygen vacancy interactions in lanthanum strontium ferrite, J. Mater. Chem. A 5 (2017) 25031.
[35] D.H. Seo, J. Lee, A. Urban, R. Malik, S.Y. Kang, G. Ceder, The structural and chemical origin of the oxygen redox activity in layered and cation-disordered Li-excess cathode materials, Nat. Chem. 8 (2016) 692–697.
[36] K. Luo, M.R. Roberts, R. Hao, N. Guerrini, D.M. Pickup, Y.S. Liu, K. Edstrom, J. Guo, A.V. Chadwick, L.C. Duda, P.G. Bruce, Charge-compensation in 3*d*-transition-metal-oxide intercalation cathodes through the generation of localized electron holes on oxygen, Nat. Chem. 8 (2016) 684–691.
[37] S. Li, X. Sun, Y. Liu, G. Liu, W. Xue, I. Waluyo, Z. Zhu, Y. Zhu, Y. Dong, Y. Huang, J. Li, Thermally aged Li-Mn-O cathode with stabilized hybrid cation and anion redox, Nano Lett. 21 (2021) 4176–4184.
[38] E. Lee, K.A. Persson, Li_xMnO_3 as a function of Li content from first-principles calculations, Adv. Energy Mater. 4 (2014) 1400498.
[39] Y. Dong, I.W. Chen, J. Li, arXiv preprint arXiv: 1908.05754 (2019).
[40] V. Esposito, D.W. Ni, Z. He, W. Zhang, A.S. Prasad, J.A. Glasscock, C. Chatzichristodoulou, S. Ramousse, A. Kaiser, Enhanced mass diffusion phenomena in highly defective doped ceria, Acta Mater. 61 (2013) 6290–6300.
[41] A. Polotai, K. Breece, E. Dickey, C. Randall, A. Ragulya, A novel approach to sintering nanocrystalline barium titanate ceramics, J. Am. Ceram. Soc. 88 (2005) 3008–3012.
[42] Y. Dong, L. Qi, J. Li, I.W. Chen, arXiv preprint arXiv:1808.05196 (2018).
[43] H. Solomon, J. Chaumont, C. Dolin, C. Monty, Zr, Y and O self diffusion in $Zr_{1-x}Y_xO_{2-x/2}$ (x=0.17), Ceram. Trans. 24 (1991) 175–184.
[44] M. Kilo, M.A. Taylor, Ch. Argirusis, G. Borchardt, B. Lesage, S. Weber, S. Scherrer, H. Scherrer, M. Schroeder, M. Martin, Cation self-diffusion of 44 Ca, 88 Y, and 96 Zr in single-crystalline calcia- and yttria-doped zirconia, J. Appl. Phys. 94 (2003) 7547–7752.
[45] D. Monceau, M. Filal, M. Tebtoub, C. Petot, G. Petot-Ervas, Kinetic demixing of ceramics in an electrical field, Solid State Ionics 73 (1994) 221–225.
[46] J.H. Park, R.N. Blumenthal, Thermodynamic properties of nonstoichiometric yttria-stabilized zirconia at low oxygen pressure, J. Am. Ceram. Soc. 72 (1989) 1485–1487.
[47] J.H. Park, R.N. Blumenthal, Electric transport in 8 mole percent Y_2O_3-ZrO_2, J. Electrochem. Soc. 126 (1979) 209–217.
[48] P.L. Chen, I.W. Chen, Grain growth in CeO_2: dopant effects, defect mechanism, and solute drag, J. Am. Ceram. Soc. 79 (1996) 1793–1800.
[49] L.A. Xue, K. Meyer, I.W. Chen, Control of grain-boundary pinning in Al_2O_3/ZrO_2 composites with Ce^{3+}/Ce^{4+} doping, J. Am. Ceram. Soc. 75 (1992) 822–829.
[50] T. Baiatu, R. Waser, K.H. Hardtl, dc electrical degradation of perovskite–type titanates: III, a model of the mechanism, J. Am. Ceram. Soc. 73 (1990) 1663–1673.
[51] T. Baiatu, Ph.D. thesis, universität karlsruhe, 1988. Detailed information at https://primo.bibliothek.kit.edu/primo_library/libweb/action/dlDisplay.do?vid=KIT&docId=KITSRC017265371&tab=kit&srt=date.
[52] O. Guillon, J. Gonzalez-Julian, B. Dargatz, T. Kessel, G. Schierning, J. Rathel, M. Herrmann, Field-assisted sintering technology/spark plasma sintering: mechanisms, materials, and technology developments, Adv. Eng. Mater. 16 (2014) 830–849.
[53] M. Oghbaei, O. Mirzaee, Microwave versus conventional sintering: a review of fundamentals, advantages and applications, J. Alloy. Compd. 494 (2010) 175–189.
[54] Y. Dong, A.T. Motta, E.A. Marquis, Atom probe tomography study of alloying element distributions in Zr alloys and their oxides, J. Nucl. Mater. 442 (2013) 270–281.
[55] C.O. De Gonzalez, E.A. Garcia, An x-ray photoelectron spectroscopy study of the surface oxidation of zirconium, Surf. Sci. 193 (1988) 305–320.